CrystEngComm

Accepted Manuscript

ROYAL SOCIETY OF CHEMISTRY

www.rsc.org/crystengcomm

Cite this: DOI: 10.1039/c0xx00000x

www.rsc.org/xxxxxx

ARTICLE TYPE

Size-controlled Wurtzite Zinc Oxide Spheres with the Characteristics of Visible Absorption and Mie Scattering

Ting-Ting Chen,[a] I-Chun Chang,[a] Min-Chiao Tsai,[a] Yi-Chun Chang,[b] Min-Han Yang,[a] Po-Chin Chen,[b] Hsin-Tien Chiu,[b] and Chi-Young Lee*[a]

Received (in XXX, XXX) Xth XXXXXXXXX 20XX, Accepted Xth XXXXXXXXX 20XX
DOI: 10.1039/b000000x

The enhancement of light harvesting efficiency over metal oxide is crucial to optics-related applications which can convert solar energy into chemical energy. Here, we demonstrated a method to develop the characteristics of visible light absorption and visible Mie scattering over wurtzite ZnO microspheres. Size-controlled ZnO microsphere were successfully prepared in thermal decomposition of amorphous/layered basic zinc salts (LBZ) spheres. Firstly, trisodium citrate was employed as the chelating agent to synthesize amorphous/LBZ microspheres in a nucleation-controlled method. The sphere size was controlled by the nuclei number which depends on the competition between hydroxyl ion and citrate to ligand with Zn^{2+}. Secondly, the visible-active wurtzite ZnO sphere was obtained by thermal decomposition. The uniform sized microspheres exhibited Mie scattering in the visible range due to the interaction with specific incident electromagnetic radiation, and the full absorption spectrum was easily obtained by tuning the size of spheres. Such uniform spheres exhibited superior visible absorption and scattering effects and thus were expected for the optics-related applications.

Introduction

The augmentation of the light utilization efficiency over metal oxide is crucial to design new solar energy conversion devices, such as dye-sensitized solar cell, [1-5] H_2 evolution, [6-8] and photocatalysis. [9-14] Various research have been focused on the promotion of light utilization efficiency. The optical band gap narrowing of metal oxide by defects or impurities has been used to promote the visible light absorption. [9, 11-16] In addition, Mie scattering effect of spherical particles was also introduced to lengthen the path of the incident light, improving the light harvesting efficiency. [4, 8, 10] Mie scattering effect is the optical phenomenon which describes the particular incident electromagnetic wave is redirected due to periodical perturbation in electron cloud of uniform spherical objects with same frequency as the electric field of the incident wave. [17-21] Theoretically, metal oxide sphere with the two optical properties can be a fascinating material to efficiently convert solar energy into chemical energy.

Recently, many studies have focused on spherical structured ZnO which is a glamorous material for various applications such as dye-sensitized solar cell,[1] photocatalysis, [10] and UV-photodetectors.[22] It was reported that the visible-active ZnO can be prepared by the thermal decomposition of zinc hydroxide/amorphous compounds. [23, 24] Sol-gel process with the assistance of chelating agents has been usually applied to synthesize zinc hydroxide/amorphous with spherical structures. The chelating agents such as trisodium citrate [25-29] and histidine [30] can form complexes with Zn^{2+} and play an important role in the morphology control. It is likely that the minority of the zinc ions are free ion which can react with hydroxyl ion to form nanoclusters. Van der Waals interactions between the surface molecules of the nanocluster as the driving force for self-assembly result in a spherical structure as reducing surface energy. [31]

However, usually it is more difficult to control the size and uniformity of metal oxide spheres than morphologies. Synthesis of zinc hydroxide/amorphous microspheres (~ 1 μm) with good uniformity and perfect spherical structures (no connection between spheres) still remained a big challenge. During reaction, the equilibrium between the solution components governs the formation of uniform colloidal particles in solution. [32, 33] It was reported that the one-step nucleation-controlled method was developed to synthesize uniform Cu_2O nanocubes with tunable size. [32] Trisodium citrate was employed as the chelating agent to form copper-citrate complex which retards the precipitation of $Cu(OH)_2$ during the addition of NaOH, resulting in the less seed number. The larger Cu_2O nanocubes were obtained by increasing the amount of sodium citrate in the reaction solution. The well-controlled particle size can be achieved through the equilibrium between OH^- and citrate to ligand with Cu^{2+}.

In this work, we demonstrated a new approach to produce size-tunable wurtzite ZnO spheres with visible light absorption and Mie scattering properties. Firstly, we adopted the nucleation-controlled method to prepare amorphous/layered basic zinc salts (LBZ) spheres with tunable sizes by using hexamethylenetetramine (HMTA) and trisodium citrate as

hydroxyl ion supplier and chelating agent, respectively. Here, the size of sphere was controlled by the concentration of HMTA, which was proportional to the nuclei number. Secondly, the amorphous/LBZ sphere was further annealed and then converted into the visible-active wurtzite ZnO sphere. Furthermore, as the spheres with uniformity could scattering specific incident light, the full absorption spectrum was easily obtained by tuning the size of spheres. The formation mechanism and optical behavior of spherical structure were systematically investigated.

Experimental

All chemicals were analytical-grade reagents and used without further purification. In a typical experiment, an aqueous solution of 15 mM zinc acetate dihydrate (Zn $(CH_3COO)_2{\cdot}2H_2O$), 6 mM trisodium citate and 40~140 mM hexamethylenetetramine (HMTA, 40, 60, 80, 100, 120, 130, and 140 mM, respectively) was refluxed at 115 ^oC for 1h. After the reflux reaction, the white powder in the solution was collected by filtering, being washed and dried in an oven at 50 ^oC and thus obtained products were named as S4, S6, S8, S10, S12, S13 and S14 respectively. The as-synthesized samples (S4, S8, S12 and S14) were further annealed at 500 ^oC for 1 h with a ramp up rate of 4 ^oC/min under air gas flow (50 sccm), and thus obtained products were named as S4a, S8a, S12a and S14a, respectively.

The morphology of the powder was investigated using a field emission scanning electron microscope (FE-SEM, Joel-6500, 15 kV) and a transmission electron microscope (TEM, JEM-ARM200FTH, 200 kV). The crystal structure of the samples was characterized by powder X-ray diffraction (Brucker D8-advanced with Cu Kα radiation λ = 1.5405981 Å). Fourier transform infrared spectrometer (FT-IR, Bruker vertex series, powder mixed with KBr and compacted to pellets) was used to measure the transmission spectra. In order to investigate the Mie scattering behavior, the powder was coated on transparent plastic slides by doctor-blade, and the UV-vis absorption spectroscope (Avantes) was utilized. The reflectance absorption spectrum of the powder was also recorded on a UV/Vis spectroscope.

Results and discussion

Characterization of amorphous/LBZ spheres

Fig. 1a-c are the SEM images of the samples S4, S12 and S14 respectively which comprise a large amount of uniform spheres. The sphere size was reduced with increasing the concentration of HMTA in reflux reaction at 115 ^oC, whereas the surface roughness increased (also see the supporting information, Fig. S1). The average diameters of sphere S4, S12 and S14 were about 1.65, 1.22 and 0.98 μm, respectively. Fig. 1a shows S4 with the largest diameter has a clean and glossy surface. In contrast, S14 with the smallest diameter displays a rough and deformed surface which was composed of irregular sheets as shown in Fig. 1c. EDS analysis shows the C, O, and Zn signals from the as-synthesized samples (Zn~15 wt%, O~34 wt%, and C~50 wt%, and EDS analysis is summarized in Table S1). The XRD patterns in Fig. S2 reveal that the crystallinity of spherical structure increased with HMTA concentration as the size of sphere was reduced. S4 (red line) is amorphous, whereas S14 (purple line) shows additional diffraction peaks located at 33.3˚ and 59.0˚.

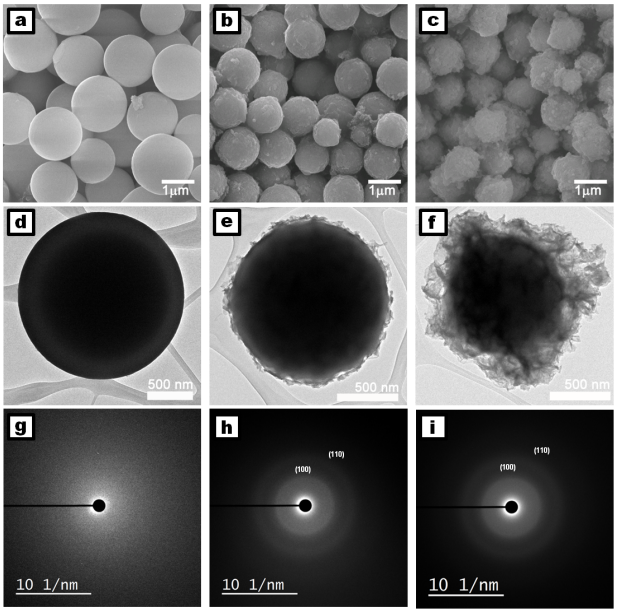

Fig. 1 SEM images of spheres (a) S4 (b) S12 (c) S14. The corresponding TEM images (d) (e) (f) and SAED (g) (h) (i).

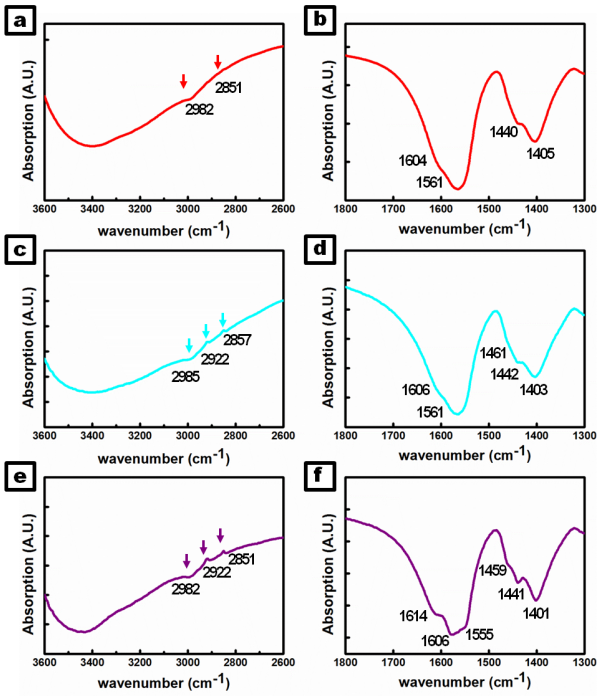

Fig. 2 FT-IR spectra of (a,b) S4 (c,d) S12 (e,f) S14.

These very weak peaks correspond to the brucite-like structure indexed as (100) and (110), implying the presence of layered basic zinc salts (LBZ).[26, 34-37] LBZ is a modified brucite structure which was composed of water molecules and inorganic or organic anions between positively charged polynuclear zinc hydroxyl layers for charge balance.[26] The broad and asymmetric peak located at 33.3^o was attributed to the disorderly stacking zinc hydroxide layers along the *a* and *b* axes which leads to destroy the symmetry of the (*hk*0) diffraction peaks.[26, 34-37]

The structural characterization obtained by using transmission electron microscopy (TEM) provides additional information

about the interior and exterior structure of these spheres as shown in the Fig. 1d-f. It was found that S4 is a ~1.8 μm diameter solid sphere with a smooth and neat surface as clearly shown in Fig. 1d. The selected area electron diffraction pattern (SAED, Fig. 1g) shows that S4 is nearly amorphous (these samples were unstable under electron irradiation) [25, 35] which is consistent with the XRD patterns. However, the TEM image of S14 presents a core-shell structure. The coarsely solid core with a diameter about 0.80 μm was coated with the irregular shell which consisted of finely thin sheets as displayed in Fig. 1f. Furthermore, the TEM analysis indicates the exterior shell exhibits a characteristic of polycrystalline structure with slight and obscure diffraction rings of (100) and (110) planes, corresponding to LBZ structure. This result agrees with the XRD pattern which displays the very weak diffraction peaks (purple line) in Fig. S2. These results indicate that the more crystalline and smaller spheres with a core-shell structure were obtained in higher concentration of HMTA.

Fig. 2 and S3 are the IR spectrum of these samples. Fig. 2a, c and e display that a broad and strong absorption band at ca. 3400 cm^{-1} is due to the stretching vibration of hydroxyl group and water. A very weak absorption band at 2850-3000 cm^{-1}, which is nearly hidden by strong absorption of hydroxyl group, can be ascribed to methyl group stretching vibration. Fig. 2 b, d and f show that strong absorption peaks at ~1600 cm^{-1} be assigned to asymmetric vibration of carboxylic group υ_{as} (COO^-). The absorption band at 1450 cm^{-1} is originated from carboxylic group symmetric vibration $\upsilon_s(COO^-)$, methyl group deformation, and hydroxyl group bending vibration. No signal was observed at the range of 1700–1720 cm^{-1} corresponding to the typical absorption bands of carbonyl group of carboxylic acid. [25, 27] It indicates that each carboxylic acid group is deprotonated. The presence of CH_2 and coordinated carboxylic group in the IR spectrum of S4 amorphous spheres suggested that citrate groups were coordinated with Zn^{2+}, which is similar to earlier studies. It was reported that the amorphous microspheres were synthesized by using zinc nitrate, HMTA, and citrate as reactants, and strong carboxylic group vibration signals in the IR spectra could be attributed to the coordinated citrate with Zn^{2+}. [25-27]

As the concentration of HMTA increasing, the additional peaks at 1459, 1614, and 2922 cm^{-1} were observed as shown in Fig. 2e and f. The IR spectrum of S14 reveals the additional peaks due to the presence of CH_3 group and coordination between carboxylic group and Zn^{2+}. It was related to the coordination of the acetate groups to Zn^{2+} in the LBZ structure. [25, 27, 35, 38] In case of S14, the exterior shell exhibits a characteristic of LBZ crystalline structure which is a construction of positively charged zinc hydroxyl layers, intercalated acetate group and water molecules. Thus, these additional peaks of $\upsilon_{as}(COO^-)$ and $\upsilon_s(COO^-)$ can be ascribed to the coordination of acetate group to Zn^{2+}, which suggested the presence of LBZ. This result agrees with the TEM image of S14 which shows clearly that disorderly LBZ shells concealed a coarsely solid core.

Proposed formation mechanism of size-controlled amorphous/LBZ spheres

According to the above observations, the sizes and morphologies of the spheres strongly depends on the concentration of reactants. [39, 40] HMTA is known as a mild basic agent to supply OH^- in the syntheses of diverse ZnO nanostructure. HMTA slowly releases OH^- during reaction, and Zn^{2+} directly reacts with OH^- to form zinc hydroxide species as the building block for crystalline ZnO rod with wurtzite phase (Fig. S4). Citrate, which is one of the common chelating agents, reacts with metal ions to form stable coordination complexes, and thus plays an important role in the formation of hierarchical structure metal oxide. In the previous studies, the amorphous random sized zinc citrate spheres and LBZ nanostructure were synthesized with addition of trisodium citrate as the chelating agent. [25-29]

In a high citrate content solution, $Zn(citrate)_2^{4-}$ complex (two equivalent citrate ions coordinate to one Zn^{2+}) is the dominated species and restrains the formation of wurtzite ZnO. [37] Moreover, the formation of Zn^{2+}-citrate complex that strongly depends on the OH^- concentration, is related to the nucleation of spheres. [25] As HMTA was added into the reaction, the released OH^- from HMTA influences the coordination between citrate and Zn^{2+} during reaction. The discharged Zn^{2+} from Zn^{2+}-citrate complex react with OH^- to form the nuclei of amorphous spheres. However, the synthesis of spheres with uniformity and tunable sizes was rarely reported in the literature.

Herein, the nucleation-controlled method was adopted to control the size of spheres. The seeding number of sphere will be controlled by the competition between OH^- and citrate ion to ligand with Zn^{2+}. As the concentration of zinc acetate and sodium citrate are fixed, the seeding number depends on HMTA concentration. The increase of the HMTA enhances the discharge of Zn^{2+}, and generates more nuclei for the spheres, leading to the formation of smaller spheres, as shown in Fig. S1. The size of the spheres was 1.65 and 0.98 μm as the HMTA concentration was 40 and 140 mM, respectively. Furthermore, the nanospheres were obtained by increasing OH^- using pre-heated HMTA (at 90 °C for 30 minutes) (Fig. S5). Briefly, sized-controlled spheres can be easily obtained by the nucleation-controlled growth using chelating agents.

The uniformity of spheres can be controlled by the distribution of chemical complex species in the solution, which depends on the molar ratio of reactants. [32, 33] The ratio of $[Zn^{2+}]$/[citrate] influence on the distribution of free and chelated Zn^{2+} in the solution, and the formation of LBZ phase.

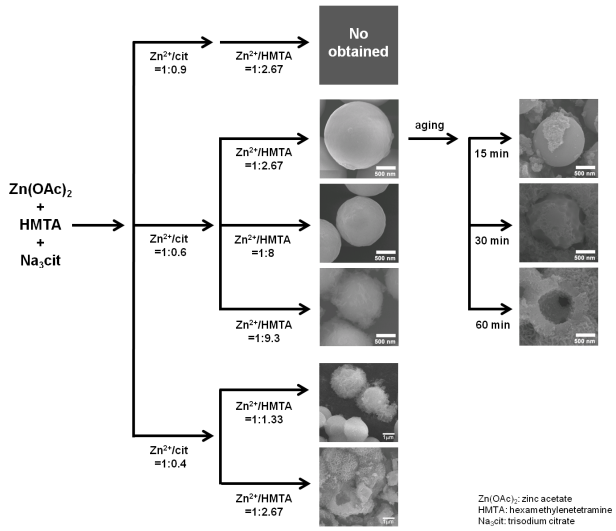

Fig. 3 Scheme of the proposed formation mechanisms of the amorphous/LBZ spherical structure.

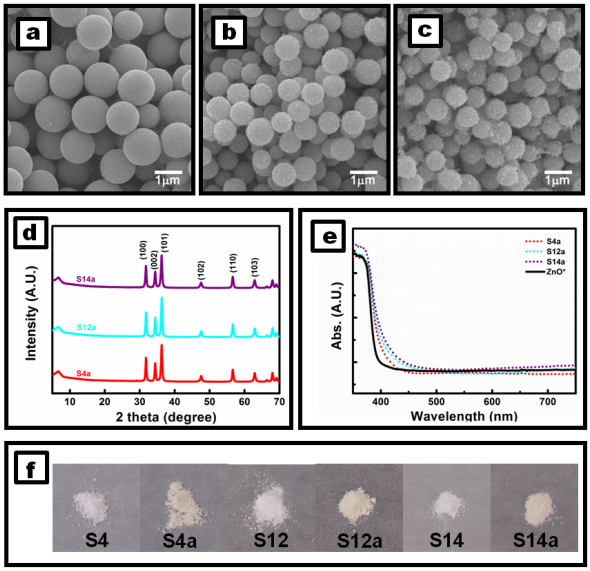

Fig. 4 SEM images of (a) S4a (b) S12a (c) S14a. (d) XRD patterns and (c) UV-vis reflectance absorption spectrum of annealed spheres. (f) photograph of various-sized spheres before and after thermal decomposition.

Fig. S6 shows the SEM images and XRD patterns of the samples synthesized with 40 mM HMTA and the Zn^{2+}/citrate molar ratio of 5. It indicates that the high Zn^{2+}/Citrate molar ratio leads to the formation of irregularly hierarchical structure with highly crystalline LBZ phase, which is unfavorable to uniformity of morphology and lead to a poor distribution of spheres.

In addition, the formation of LBZ sheets was further studied in detail. It was reported that amorphous spheres serve as native templates and sacrifice for the formation of crystalline metal oxide/hydroxide hierarchical structure through Ostwald ripening process. [27, 28, 41] Under high HMTA concentration (> 80 mM), the spheres with LBZ exterior shell and amorphous interior solid core were obtained. During the reaction, the unstable amorphous spheres become a template for hierarchical structure of LBZ. Dissolution of amorphous spheres from the smooth surface followed by the deposition of crystalline LBZ sheets proceeds spontaneously. During a further aging at 90 °C for 60 min, an amorphous solid sphere was etched gradually and continuously from surface and finally transformed to a hollow sphere which is consisted of LBZ sheets only (Fig. S7). A schematic diagram of the proposed formation mechanism of amorphous/LBZ spherical structure has been displayed as in Fig. 3.

Thermal decomposition of amorphous/LBZ Spheres

In general, thermal decomposition of metal hydroxide results in the formation of metal oxides without morphological change, and has been used to synthesis crystalline metal oxide sphere. [23, 24, 35] The thermal behavior of the amorphous/LBZ sphere decomposed into ZnO was investigated by TGA. The TGA profiles of samples presented in Fig. S8a, show that the mass of the samples keeps a constant value at ~380 °C. A gradual weight loss at temperatures below 300 °C is related to the dehydration of physically adsorbed water, and the weight loss at ~350 °C was attributed to removal of organic content.

The amorphous/LBZ sphere, S4, S12, and S14 were annealed at 500 °C for 1 h under air flow, and thus obtained products were named as S4a, S12a, and S14a respectively. Fig. 4a-c shows that all the spheres remained in spherical shape but shrunk in size. The average diameters of sphere S4a, S12a and S14a were about 1.21, 0.81 and 0.74 μm, respectively. The crystalline structure of the samples was further characterized by XRD. The XRD diffraction patterns in Fig. 4d reveal that all the annealed samples are highly crystalline with the characteristic diffraction peaks at 31.7°, 34.4° and 36.2°, which correspond to the wurtzite phase (JCPDS 36-1451) and indexed as (100), (002) and (101), respectively. The average grain sizes of S4a, S12a and S14a are 24.9 nm, 26.8 nm and 23.0 nm respectively, determined by using Scherer's formula. Fig. S8b displays the TEM image of S4a. A solid sphere with polycrystalline wurtzite ZnO was evidenced by the inset SAED pattern with the three major planes {100}, {002} and {101}. Fig. S8c shows the Raman spectra of ZnO spheres. The fundamental modes at ~330, 380, 438 , 560 and 580 cm^{-1} are assigned to the E_2^{high}-E_2^{low}, A_1(TO), E_2^{high} , A1 (LO) and E_1 (LO) of wurtzite ZnO, respectively.[31, 42] Especially, the E_1 (LO) mode caused by the formation of defects such as oxygen vacancy, zinc interstitial or these complexes reveals the presence of defects in the ZnO spheres.[42]

The ZnO spheres powder showed a color of yellow cream after annealing, and their UV-vis reflectance absorption spectra were displayed in Fig. 4e and f. The obvious band tail in 400~500 nm observed for all ZnO spheres corresponds to the visible light absorption. This absorption can be originated from defects (EDS analysis yielded the O and Zn signals and thus the effect of impurity can be neglected).[42] The type of defects in ZnO spheres was subsequently investigated in further detail using Photoluminescence (PL) spectroscopy. Fig. S8d presents the PL spectrum of samples with a He-Cd laser excitation (325 nm). The strong and broad green emission at ~525 nm is typically associated with oxygen vacancies, whereas the sharp emission at ~382 nm is attributed to the band edge transition.[43] The presence of oxygen vacancies can be responsible for the band tail and the enhancement of the visible light absorption of the ZnO.

Mie scattering behavior of amorphous/LBZ spheres

Inorganic spherical structure with the diameter of about 1 μm exhibits interesting optical properties. As the size of a spherical object approaches the wavelength of incident light, the resonance effect takes place, and is mainly confined to the surface of the object, known as Mie's scattering. [18-21]

Fig. 5 Photographs of transparent plastic slides which were coated with various-sized spheres by doctor-blade. (a) All spheres synthesized with different concentration of HMTA (40-140 mM) have white color which is similar to general ZnO powders. (b) When turn on a back light, multicolored words could be observed through the transparent plastic slides by Mie scattering at scattering angle θ > 0 ° (from left to right, red (S4), orange (S6), yellow (S8), green (S10), cyan (S12), blue (S13), and purple (S14), respectively).

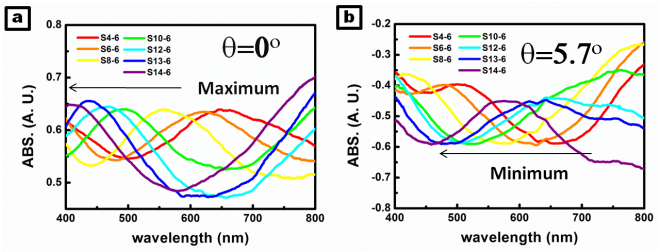

Fig. 6 UV-vis absorption spectrum of various-sized spheres synthesized with different concentration of HMTA (40-140 mM) at different scattering angles (a) θ = 0 ° (b) θ =5.7°.

Fig. 5a shows a photograph of a transparent plastic film that was coated with various sized spheres, displaying white in color as common ZnO powder. When turning on a back light, different vivid colors were observed due to the light scattering by the spheres as shown in Fig. 5b (scattering angle > 0°). The coated plastic film with powder of S4, S6, S8, S10, S12, S13, and S14 displayed red, orange, yellow, green, cyan, blue, and purple in color respectively. The full absorption spectrum can be achieved by tuning the size of spheres.

According to the literature, the forward scattering of incident light, namely, zero angle scattering (scattering angle = 0°) by amorphous TiO_2 spheres was determined by the local minimum of absorption in UV-vis spetra. [20] In order to understand more details about scattering properties of these spheres, UV-vis spectra were utilized to interpret the colors we observed from the coated transparent plastic films. Fig. 6a and b are absorption spectra of spheres at scattering angle θ = 0° and 5.7°, respectively. Apparently wave-like curves, illustrated in Fig. 6, give strong evidence for the highly uniformity of spheres in this work. Otherwise, the spectra presented as flat lines instead of wave-like curves with size polydispersity over 10%. [19]

The angular dependence of Mie scattering influences the local absorption minimum at different scattering angles in the spectra. For example, Fig. S9a are the absorption spectra of S4 at scattering angle θ = 0° and 5.7°. The wavelength of forward scattering of incident light (scattering angle = 0°, solid line, in Fig S9a) by S4 spheres is about ~500 nm which was determined by the local minimum of absorption in UV-vis spectrum. The enhancement in light intensity of ~500 nm in the forward direction results from the resonance between the S4 and the incident light with wavelength of~500 nm. It leads to the local minimum of absorption in the UV-vis spectra. Thus, blue color was observed due to the light scattering by S4 when turning on a back light with scattering angle = 0° (It was very difficult to take a good picture due to the very strong incident light). As increasing of the scattering angle, the decreased flux of the forward scattering light leads to the increase of absorption. The local minimum absorption in UV-vis spectrum (scattering angle = 5.7°, dash line, in Fig S9a) locates at about ~650 nm that is corresponding to red color. This is consistent with the picture in Figure 3b (letter "N").

The degree of scattering depends not only on the scattering angle but also on the size of spheres. As shown in the Fig. 6b, the spheres with an average diameter of 1.65 μm, 1.20 μm and 0.94 μm obtained with the addition of 40 mM, 120 mM and 140 mM HMTA scattered ca. 650, 500 and 425 nm light and displayed red, blue and purple in colors at the low incident angle (letter "N", "M" and "E" in Fig 5b), respectively. In addition, as the size of spheres decrease, a blue-shift in local minimum and maximum of absorption was observed in Fig. 6a and b, respectively. The theoretical Mie scattering spectra of spheres were calculated by Mie Plot software [20,44] and presented in the Fig. S10. The simulated curves match the experimental spectra well, although there is a small inconsistency for smaller spheres (S13 and S14) due to deformed spherical structure with the irregular shell of LBZ.

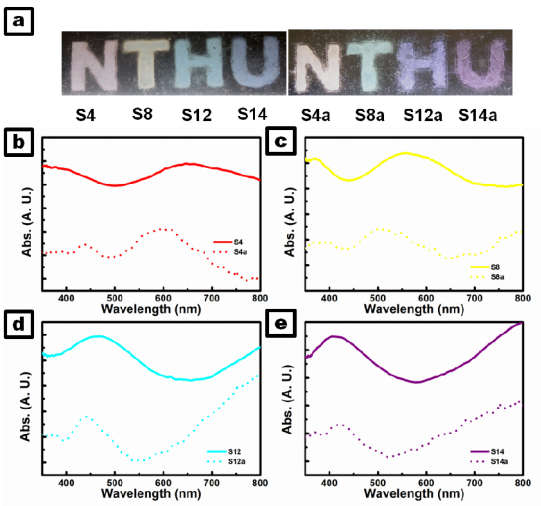

Fig. 7 (a) photograph of various-sized spheres before and after annealing. When turn on a back light, vivid words were still observed through the transparent plastic slides by Mie scattering at scattering angle θ > 0 °. UV-vis transmittance absorption spectrum of annealed spheres (b) S4a (c) S8a (d) S12a (e) S14a powder coated on transparent plastic slides (θ = 0°).

Mie scattering behavior of ZnO spheres

As mentioned above, the annealed spheres remained the spherical structure but exhibited the crystallinity of wurtzite phase. The reduced volume and the increased refractive index of spheres had influences on the Mie scattering properties. As shown in Fig. 7a, the vivid color was still observed when the samples were lighted under a back light, implying that these ZnO spheres had Mie scattering property as well. The plastic film coated with S4a, S8a, S12a and S14a displayed orange, blue, purple and violet in colors at the low incident angle, respectively. Fig. 7b-e are the absorption spectra of S4a, S8a, S12a and S14a at scattering angle θ = 0 °, respectively. The ZnO spheres with an average diameter of 1.21 μm (S4a) forward scattered the light with wavelength ca. 490 and 775 nm (S4: ~ 500 and 880 nm). It was found the slightly blue shift of local minimum in the absorption spectra of these spheres after thermal decomposition. It is originated from the shrink sphere volume (reduced 30% diameter) and the increased refractive index.

Light harvesting is the key factor for the new solar energy conversion devices. It was reported that the TiO_2 with Mie scattering effect has been applied in the dye-sensitized solar cells [4] and photoelectrochemical H_2 production,[8] to enhance the light utilization efficiency over TiO_2. The lengthened path of the incident light was induced by scattering effect between uniform TiO_2 spheres with size comparable to its wavelength. Therefore, ZnO spheres with the characteristics of visible light absorption

and scattering is expected to be useful in optical-related applications to increase light harvesting. Moreover, the feature of light selectivity of Mie scattering can also be used in SERS enhancement,[45] and biosensor.[17] The further studies regarding this are in progress.

Conclusions

In summary, we successfully synthesized the size-tunable wurtzite ZnO spheres with visible light absorption and scattering properties in a two-step method. Firstly, the nucleation-controlled method with the assistance of the chelating agent was adopted to control the size of amorphous/LBZ spheres by adjusting HMTA concentration in a reflux reaction. The competition between hydroxyl ion and citrate to ligand with Zn^{2+} has an influence on the size, uniformity and the crystal phase of spheres. Secondly, the amorphous/LBZ spheres were further annealed and transformed into the wurtzite ZnO spheres with visible absorption. The uniform spheres exhibits Mie scattering behavior in the visible range, and the full absorption spectrum was easily obtained by tuning the size of spheres. The fascinating optical property of ZnO spheres was expected for the optical-related applications, such as SERS enhancement, dye-sensitized solar cell, and H_2 evolution by increasing light harvesting.

Acknowledgements

The authors would like to thank the National Science Council of the Republic of China, Taiwan, for financially supporting this research under Contract No. NSC 101-2113-M-007-012-MY3. Shalini Jayakumar is appreciated for her editorial assistance.

Notes and references

[a] *Department of Materials Science and Engineering, National Tsing Hua University, Hsinchu 30013, Taiwan, R. O. C.*
E-mail: cylee@mx.nthu.edu.tw
[b] *Department of Applied Chemistry, National Chiao Tung University, Hsinchu 30010, Taiwan, R.O.C.*
Electronic Supplementary Information (ESI) available. See DOI: 10.1039/b000000x/
† Electronic Supplementary Information (ESI) available: [details of any supplementary information available should be included here]. See DOI: 10.1039/b000000x/

References

1. Z. Dong, X. Lai, J. E. Halpert, N. Yang, L. Yi, J. Zhai, D. Wang, Z. Tang and L. Jiang, *Adv. Mater.*, 2012, **24**, 1046-1049.
2. V. M. Guerin, J. Elias, T. T. Nguyen, L. Philippe and T. Pauporte, *Phys. Chem. Chem. Phys.*, 2012, **14**, 12948-12955.
3. H. Wang, M. Miyauchi, Y. Ishikawa, A. Pyatenko, N. Koshizaki, Y. Li, L. Li, X. Li, Y. Bando and D. Golberg, *J. Am. Chem. Soc.*, 2011, **133**, 19102-19109.
4. I. G. Yu, Y. J. Kim, H. J. Kim, C. Lee and W. I. Lee, *J. Mater. Chem.*, 2011, **21**, 532-538.
5. Q. Zhang, D. Myers, J. Lan, S. A. Jenekhe and G. Cao, *Phys. Chem. Chem. Phys.*, 2012, **14**, 14982-14998.
6. K. Maeda, T. Takata, M. Hara, N. Saito, Y. Inoue, H. Kobayashi and K. Domen, *J. Am. Chem. Soc.*, 2005, **127**, 8286-8287.
7. S. C. Warren and E. Thimsen, *Energy Environ. Sci.*, 2012, **5**, 5133-5146.
8. H. Xu, X. Chen, S. Ouyang, T. Kako and J. Ye, *J. Phys. Chem. C*, 2012, **116**, 3833-3839.
9. S. Liu, C. Li, J. Yu and Q. Xiang, *Crystengcomm*, 2011, **13**, 2533-2541.
10. F. Wang, D. Zhao, Z. Xu, Z. Zheng, L. Zhang and D. Shen, *J. Mater. Chem. A*, 2013, **1**, 9132-9137.
11. J. Wang, Z. Wang, B. Huang, Y. Ma, Y. Liu, X. Qin, X. Zhang and Y. Dai, *ACS Appl. Mater. Interfaces*, 2012, **4**, 4024-4030.
12. S. Baruah, S. S. Sinha, B. Ghosh, S. K. Pal, A. K. Raychaudhuri and J. Dutta, *J. Appl. Phys.*, 2009, **105**, 074308-1-074308-6.
13. S. Rehman, R. Ullah, A. M. Butt and N. D. Gohar, *J. Hazard. Mater.*, 2009, **170**, 560-569.
14. M. Kong, Y. Li, X. Chen, T. Tian, P. Fang, F. Zheng and X. Zhao, *J. Am. Chem. Soc.*, 2011, **133**, 16414-16417.
15. J. Cao, Y. Zhang, L. Liu and J. Ye, *Chem. Commun.*, 2013, **49**, 3440-3442.
16. Q. Kang, J. Cao, Y. Zhang, L. Liu, H. Xu and J. Ye, *J. Mater. Chem. A*, 2013, **1**, 5766-5774.
17. M.-C. Tsai, T.-L. Tsai, D.-B. Shieh, H.-T. Chiu and C.-Y. Lee, *Anal. Chem.*, 2009, **81**, 7590-7596.
18. G. N. Plass, *Appl. Opt.*, 1964, **3**, 867-872.
19. P. D. García, R. Sapienza, J. Bertolotti, M. D. Martín, Á. Blanco, A. Altube, L. Viña, D. S. Wiersma and C. López, *Phys. Rev. A*, 2008, **78**, 023823.
20. M. C. Tsai, T. L. Tsai, C. T. Lin, R. J. Chung, H. S. Sheu, H. T. Chiu and C. Y. Lee, *J. Phys. Chem. C*, 2008, **112**, 2697-2702.
21. M. Retsch, M. Schmelzeisen, H.-J. r. Butt and E. L. Thomas, *Nano Lett.*, 2011, **11**, 1389-1394.
22. M. Chen, L. Hu, J. Xu, M. Liao, L. Wu and X. Fang, *Small*, 2011, **7**, 2449-2453.
23. M.-C. Wu and C.-S. Lee, *Inorg. Chem.*, 2006, **45**, 9634-9636.
24. L. Zhu, Y. Zheng, T. Hao, X. Shi, Y. Chen and J. Ou-Yang, *Mater. Lett.*, 2009, **63**, 2405-2408.
25. S. Cho, J.-W. Jang, A. Jung, S.-H. Lee, J. Lee, J. S. Lee and K.-H. Lee, *Langmuir*, 2010, **27**, 371-378.
26. P. Gerstel, R. C. Hoffmann, P. Lipowsky, L. P. H. Jeurgens, J. Bill and F. Aldinger, *Chem. Mat.*, 2005, **18**, 179-186.
27. Q. Xie, J. Li, Q. Tian and R. Shi, *J. Mater. Chem.*, 2012, **22**, 13541-13547.
28. N. Tripathy, R. Ahmad, H.-S. Jeong and Y.-B. Hahn, *Inorg. Chem.*, 2011, **51**, 1104-1110.
29. Z. Xia, Y. Wang, Y. Fang, Y. Wan, W. Xia and J. Sha, *J. Phys. Chem. C*, 2011, **115**, 14576-14582.
30. Q. Wu, X. Chen, P. Zhang, Y. Han, X. Chen, Y. Yan and S. Li, *Cryst. Growth Des.*, 2008, **8**, 3010-3018.
31. G. Zhang, X. Shen and Y. Yang, *J. Phys. Chem. C*, 2011, **115**, 7145-7152.
32. I. C. Chang, P.-C. Chen, M.-C. Tsai, T.-T. Chen, M.-H. Yang, H.-T. Chiu and C.-Y. Lee, *Crystengcomm*, 2013, **15**, 2363-2366.
33. M. Ocaña, R. Rodriguez-Clemente and C. J. Serna, *Adv. Mater.*, 1995, **7**, 212-216.
34. H. Morioka, H. Tagaya, M. Karasu, J.-i. Kadokawa and K. Chiba, *Inorg. Chem.*, 1999, **38**, 4211-4216.
35. R. Q. Song, A. W. Xu, B. Deng, Q. Li and G. Y. Chen, *Adv. Funct. Mater.*, 2007, **17**, 296-306.
36. G. G. C. Arizaga, K. G. Satyanarayana and F. Wypych, *Solid State Ion.*, 2007, **178**, 1143-1162.
37. Z. Xia, J. Sha, Y. Fang, Y. Wan, Z. Wang and Y. Wang, *Cryst. Growth Des.*, 2010, **10**, 2759-2765.
38. A. S. Milev, G. S. K. Kannangara and M. A. Wilson, *Langmuir*, 2004, **20**, 1888-1894.
39. T. Zhang, W. Dong, M. Keeter-Brewer, S. Konar, R. N. Njabon and Z. R. Tian, *J. Am. Chem. Soc.*, 2006, **128**, 10960-10968.
40. K. Govender, D. S. Boyle, P. B. Kenway and P. O'Brien, *J. Mater. Chem.*, 2004, **14**, 2575-2591.
41. S. Inoue and S. Fujihara, *Inorg. Chem.*, 2011, **50**, 3605-3612.
42. J. Wang, Z. Wang, B. Huang, Y. Ma, Y. Liu, X. Qin, X. Zhang and Y. Dai, *ACS Appl. Mater. Interfaces*, 2012, **4**, 4024-4030.
43. H. Zeng, G. Duan, Y. Li, S. Yang, X. Xu and W. Cai, *Adv. Funct. Mater.*, 2010, **20**, 561-572.
44. S. M. Scholz, R. Vacassy, J. Dutta, H. Hofmann and M. Akinc, *J. Appl. Phys.*, 1998, **83**, 7860-7866.

45. A. Zenidaka, T. Honda and M. Terakawa, *Appl. Phys. A-Mater. Sci. Process.*, 2011, **105**, 393-398.

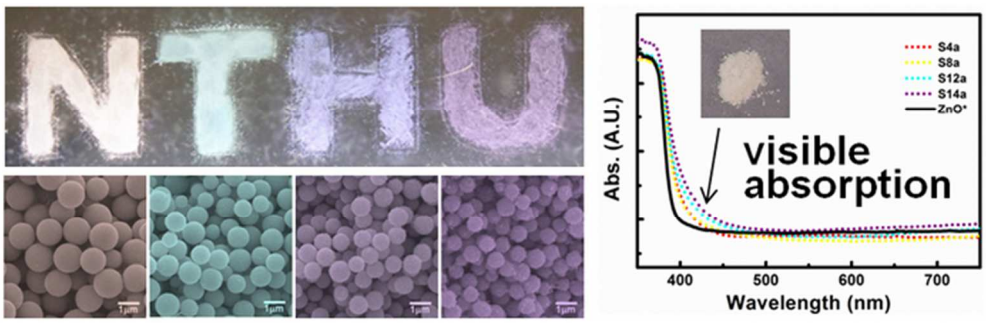

119x38mm (150 x 150 DPI)